Rock Mechanics and Rock Engineering (2022) 55:2597–2613
https://doi.org/10.1007/s00603-021-02626-5

ORIGINAL PAPER

A New Dynamic Indentation Tool for Rapid Mechanical Properties Profiling and Mapping

Jesse C. Hampton[1] · **Gregory N. Boitnott**[2] · **Laurent Louis**[2]

Received: 21 January 2021 / Accepted: 16 August 2021 / Published online: 2 September 2021

Abstract

Surface measurements are used extensively in many industries and research disciplines to characterize a material's mechanical properties and strength without the need for traditional, time consuming, and expensive laboratory tests, or for large volumes of sample material. This paper briefly reviews indentation methodologies for index and physical properties measurements and then focuses on the implementation of a method of using the measured force versus time of an impact to infer mechanical properties. By relying only on the measurement of force versus time, the method greatly simplifies the measurement process and thus allows for applications requiring rapid and automated measurements of both elastic stiffness and/or inelastic deformation during indentation. The indenter tip geometry, free-fall height, and the mechanical model used to describe the interaction of the contact between the indenter and material are investigated through the analysis of measurements performed on a wide variety of materials including plastics, rocks, ceramics, and asphalt. It is shown that using a spherical tip the method can be used to provide measurements of the elastic stiffness by fitting the measured force versus time curves to predictions of quasi static elastic theory. We then show how conversion of the force–time data into force–displacement curves realizes a direct connection with the already established static indentation interpretation framework. Through the use of force–displacement interpretation, the method becomes applicable to arbitrary tip geometries and inelastic mechanical properties. Through illustrative examples, we show how the force–displacement data from an impact can be interrogated for critical parameters such as loading and unloading characteristics, and maximum, residual, and elastic displacement.

Keywords Automated method · Indentation · Elastic stiffness · Inelastic deformation

1 Introduction

Physical properties, and specifically elastic properties, are required for most sub-disciplines of geological engineering when efforts to constrain rock behavior are pursued. Decades of research have been dedicated to the study of experimental rock properties and the relationship between laboratory-measured physical properties and in-situ geologic behavior (Tutuncu et al. 1998; Tutuncu 1998; Chang et al. 2006; Pimienta et al. 2015). In civil engineering applications, experimental determination of elastic properties, such as Young's modulus, aids in structural design, slope stability determination, tunneling, underground construction, and mining (Choens and Chester 2018; Gutierrez et al. 2014). Similarly, the determination of rock properties in oil and gas operations is critical for safe, reliable, and efficient hydrocarbon extraction from both conventional and unconventional reservoirs (Abid and Geng 2020; Vernik and Liu 1997; Bayuk et al. 2008; Graham et al. 2020; Chen et al. 2015). Deep earth geothermal operations also require critical information of rock properties to design and manage productive heat exchange systems (Reinisch et al. 2018; Liu et al. 2018).

Geothermal and oil and gas operations typically make engineering designs with very limited characterization of geomechanical properties from core data due to the financial limitations to acquire core materials from even a small fraction of drilled wells. Even when core materials are acquired, approved budgets for physical properties measurements are often a fraction of the core acquisition costs, resulting in

✉ Jesse C. Hampton
jesse.hampton@wisc.edu

[1] Geomechanics and Damage Group (GeoD), Department of Civil and Environmental Engineering, University of Wisconsin-Madison, 2206 Engineering Hall, 1415 Engineering Drive, Madison, WI 53706, USA

[2] New England Research, Inc, 331 Olcott Drive, STE L1, White River Junction, VT 05001, USA

fewer measurements than oftentimes necessary to properly sample and constrain the anisotropy and heterogeneity in mechanical properties (Geng et al. 2017; Keir et al. 2011; Louis et al. 2012, 2005; Sams 1995; among many others). Due to these logistical constraints, methods are needed that enable rapid and low-cost mechanical properties characterization of large volumes of core.

Material hardness measurements via indentation methods has a long and rich history spanning many decades of academic research and industrial development (Samuels and Mulhearn 1957; Darrow et al. 1969; Gilman 1975; Perrott 1977; Oliver and Pharr 1992). The desire to measure hardness and other physical properties from surface measurements is ubiquitous: disciplines related to ceramics, plastics, metals, composites, wood, civil engineering materials (e.g., concrete and cement), and geologic materials, among many others, all benefit from non-destructive surface measurements, including indentation. Instrumented indentation measurements spanning many length scales has advanced such that high-fidelity acquisitions of force data can be readily acquired throughout indentation measurements regardless of loading frequency, while indenter tip displacement into the specimen material is typically much more readily acquired throughout slow displacement rate indentation procedures.

In this paper, we describe and test a new dynamic indentation technique which operates at the millimeter-scale and avoids the need for direct measurements of displacement. The method relies only on the measurement of force versus time during the impact between an instrumented impactor and a sample. Applied repeatedly as a function of position, the method can be used to map or profile mechanical variations along the surface of a heterogeneous material. A benefit to this new instrumented dynamic impact measurement process is that imaging/measurement of the indentation is not necessary for mechanical properties determination. This allows many thousands of measurements to be made such that information on mechanical properties and variability can be rapidly determined for a large interval (e.g., hundreds of meters of core material at centimeter spacing). Adjustable parameters of the experimental setup can produce measurements of mechanical responses ranging from purely elastic to strongly inelastic. The goal of these measurements is to efficiently constrain elastic properties and characterize inelastic processes using an automated process.

In the first section, the standard static indentation technique is briefly reviewed to serve as a reference for the interpretation of the dynamic method. Then, the theory of the dynamic indentation is laid out within the framework of its original development which assumes elastic contact interaction between the impactor and the measured material. The response of the tool is illustrated on a range of materials including plastics, ceramics, a shale core section, and asphalt. Based on the observation that significant deviation from elastic behavior is commonly observed, a more in-depth analysis of the tool response is proposed which recasts the experimental data in terms of force vs. displacement. This later approach takes advantage of previous knowledge regarding the acquisition and interpretation of static indentation data.

It is shown that the dynamic indentation method introduced here enables high-throughput mechanical profiling and mapping without the need to compromise on the quality of the outputs, which is beneficial for heterogeneous geologic and engineering materials characterization across large spatial intervals. While this investigation is performed through the primary lens of geological engineering as one potential application, more general material science applications such as parts production in manufacturing should also be considered.

2 Review of the Static Indentation Method

2.1 Elastic Stiffness and Inelastic Deformation

Micro- and nanoindentation techniques have been extensively studied in the literature where advances in the experimental and analysis techniques have given rise to high accuracy measurements of elastic properties (Oliver and Pharr 1992, 2003; Fischer-Cripps 2007; Mazeran et al. 2012; Field et al. 2003; Hull et al. 2017; Oyen and Cook 2009; Shukla et al. 2013; Hay and Pharr 1998). Static indentation methods to determine elastic and inelastic properties are well known and research has progressed for several decades. In general, indentation is a relatively simple method where a material of interest with unknown mechanical properties, such as elastic modulus and hardness, is contacted with another material with known physical properties (Fischer-Cripps 2007). Many static indentation techniques, such as Brinell, Knoop, Vickers, and Rockwell tests are similar to nanoindentation measurements, whereas the main differences are the scale of indentation and the method in which the contact area is measured. Traditionally, larger scale indentation techniques are accompanied with direct imaging of the residual impression on the specimen, while nanoindentation relies heavily on accurate displacement measurements to calculate the contact area at several points along the loading curve. Though considerable advances in imaging technology have been applied since the advent of nanoindentation measurements, indirectly determining the contact area via accurate displacement measurements is still the main analysis method for nanoindentation research. Displacement measurements for static indentation methods are made possible via the high-fidelity acquisition of various styles of displacement

transducers, e.g., linear variable displacement transducer, laser positioning, or other methods.

Figure 1 (left) shows a force–displacement curve for a generic nanoindentation measurement, where the loading and unloading segments are identified, along with several key parameters such as P_{max}, unloading slope (S), h_f, and h_{max}. P_{max} and h_{max} refer to the maximum load and displacement, respectively. h_f is the final displacement, or permanent displacement after the indenter is fully unloaded. Final displacement is also referred to as residual displacement, h_r, in many references. Figure 1 (center) and (right) show schematic representations of a spherical and a Berkovich indenter, respectively. Following Fig. 1 (right) (Berkovich indenter), the depth along which full contact is made between the indenter and the specimen is described as:

$$h_c = h_{\max} - \in \frac{P_{\max}}{S} \tag{1}$$

where, S is the unloading slope (Fig. 1 (left)) of the initial linear region of the force–displacement curve, $\in$ is a constant that depends on the geometry of the indenter, with typical values between 0.72 and 1; 0.75 for this study due to using spherical and cube corner indenter geometries (Fischer-Cripps 2007; Oliver and Pharr 1992). For spherical indenters, h_c is determined by $h_{max} - h_e/2$, where h_e is termed the elastic displacement and is defined as $h_{max} - h_f$.

The contact area is described by:

$$A = F\left(h_c\right) \tag{2}$$

where this area function, or indentation shape function, must be carefully determined. Geometrical detail is especially important in nanoindentation measurements using sharp indenters because the indenter tip is often machined or ground and will not be perfectly sharp (Oliver and Pharr 2003). This issue is lessened when the indenter is scaled-up to micro and millimeter scale tips because of advanced manufacturing methods and the influence of the indenter tip is lessened as indentation depth is increased. Contact area shape functions for various indenter geometries can be found in Fischer-Cripps (2007). After the contact area is determined via h_c, a hardness value can be estimated from $H = P_{max}/A$. Scrutiny should be given to comparisons of hardness from differing techniques, as this hardness value is determined via the area in contact during loading, while many traditional hardness measurements are determined via the residual indentation geometry, $H = f(P_{max}, h_r)$.

The indentation modulus (often referred to as reduced Young's modulus), E^*, can be described by:

$$E^* = \frac{\sqrt{\pi} \cdot S}{2 \cdot \beta \cdot \sqrt{A}} \tag{3}$$

where S is the unloading stiffness (dP/dh). In common practice, the unloading stiffness is determined by the most linear region immediately following the maximum force/displacement condition. β is a dimensionless shape correction factor having physical meaning derived from the indenter shape and physical processes associated with elastic-inelastic deformation of various geometry indenters, e.g., 1 for spherical indenters and 1.034 for cube corner indenter geometries (Oliver and Pharr 2003).

2.2 Limitations of Traditional Static Indentation Workflows

Advancements in imaging and image processing techniques have greatly facilitated the extraction of geometry parameters of final indentations, but these techniques still take considerable time and are impractical for large-scale measurement programs where many measurements are required. Improvements in sensing technology delivering more reliable force and displacement measurements have lessened the need for imaging of the final indentation geometry, but

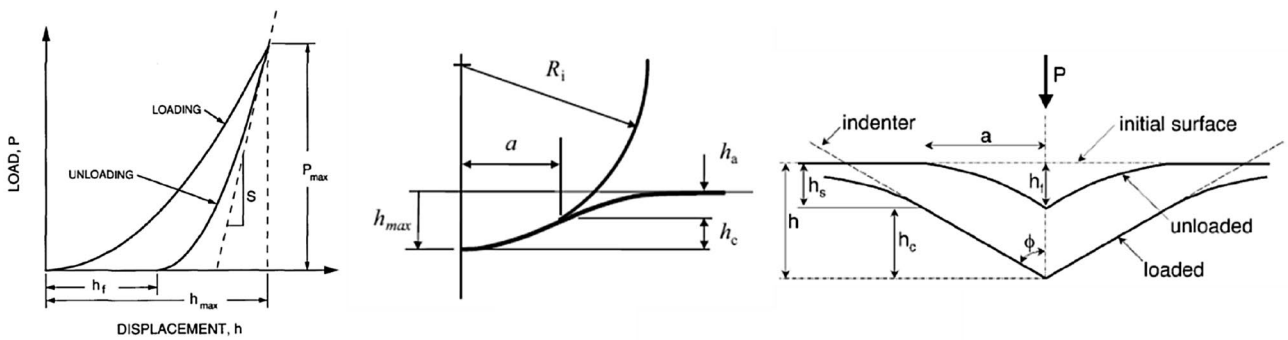

Fig. 1 Left: schematic representation of a load–displacement curve for an indentation experiment (Oliver and Pharr 1992). Center: schematic of contact between a rigid and spherical indenter and a flat specimen (Fischer-Cripps 2007). Right: schematic of a sharp indenter contact geometries at maximum depth and after unloading (Oliver and Pharr 2003)

accurate determination of the properties of inelastic, anisotropic, and heterogeneous materials remains a challenge. Some of these issues specifically arise with small-scale (nanometer and micrometer length scales) physical measurements in natural materials where pore size, grain size, and sample preparation can substantially impact the results. In the case of nanoindentation, the measurement typically requires surface preparation techniques that produce very flat surfaces (e.g., ion milling), to minimize the mechanical effect of any surface irregularities. In many cases, however, this does not correct for the very strong heterogeneity present at the grain scale (variety of minerals with hard to control surface characteristics and multiple interfaces), nor the fact that the volume probed may not constitute a representative elementary volume (REV) for the material investigated. Indeed, nanoindentation measurements are often limited by the fact that the measurement is conducted with a set force under the assumption of material self-similarity, whereas it has been shown in shale rock for instance that both reduced modulus and hardness vary greatly as a function of applied force before stabilizing when an REV is reached. Finally, the presence of creep in static measurements constitutes an added complexity which can again negatively impact the robustness of the result if not accounted for.

In the work described here, some of these issues can be inherently attenuated by the fact that the tool operates in a dynamic manner, and probes volumes that are orders of magnitudes larger than the ones typically seen by nanoindentation, hence avoiding the REV issue in most cases. Regarding surface condition, while it still remains a variable influencing the measurements and thus must be considered in general practice, satisfactory results are obtained with only limited surface preparation involving basic diamond rotary saws (rocks and asphalt), milling (soft plastics), and surface grinding (hard plastics and ceramic). In general, it is an objective of this work to ensure that the developed measurement and analysis techniques can be applied without significant sensitivity to surface finish at this level.

3 Instrumented Dynamic Indentation

The principle of dynamically testing a rock surface to infer some mechanical property is already employed in a type of measurement that can be loosely termed rebound hardness. Examples include LEEBS, Shore Scleroscope, and Schmidt Hammer. Unlike indentation methods, rebound hardness methods have the advantage that they are easily transportable and produce a simple output quantifying the fractional energy loss during impact that results in rapid measurements at a local point in a material. These methods are however limited in that they cannot be used in the case of purely elastic impact (e.g., no energy loss) and they cannot distinguish or resolve the mechanisms active in causing the observed energy loss. Thus, they are limited to applications as index measurements that must be applied through correlations with desired mechanical properties such as stiffness and strength.

The technique discussed in this study extends the concept of rebound hardness by adding a continuous measurement of the force as a function of time throughout the impact (Boitnott et al. 2014, Rathbun et al. 2014, Gramin et al. 2016). The experimental configuration is shown in Fig. 2. The indenter mass, tip geometry, and drop height are all user prescribed and known quantities. Attached to the indenter tip are high frequency force and acceleration transducers that allow for the recording of each impact of the free-falling indenter assembly using a digital oscilloscope. For the experiments described here, a mass of approximately 70 g is used for the indenter assembly. In this configuration, adjustments of drop height and tip geometry can be targeted for keeping the indenter impact in the elastic range (e.g., a blunt spherical tip) or for specifically causing sub-millimeter scale inelastic deformation (e.g., a sharp cube corner tip) depending on the goals of the measurement and the specimen's mechanical properties. The adjustability of indenter mass, drop height, and tip geometry allows one to target the amount and scale of inelastic deformation allowable for a particular application.

For a spherical indenter tip and a drop height selected to stay within an elastic regime, a Hertzian contact model can be used to describe the response (Johnson 1987). Figure 3 shows repeat measurements of elastic impacts on two materials with significantly different stiffnesses (plastic and ceramic). The repeatability of the measurements for these end member materials illustrates the range of signals generated during measurements on stiff (short time and high force) and compliant (longer time and lower peak force) samples. Though the acquisition of high-fidelity force–time information throughout a dynamic impact can be readily extracted, there are several potential sources of uncertainty that can contribute to the interpretation of the measured force versus time function. In practice, two main sources of uncertainty are (1) the assumption of a known impact velocity; and (2) the treatment of the specimen material as an infinite mass, e.g., zero velocity condition for the specimen during impact.

For elastic measurements, a Hertzian contact model can describe the force–time response during the impact via the derivations of Hertz (1882) as summarized by Johnson (1987). In the absence of external forces and neglecting dynamic effects (e.g., elastic waves), elastic theory predicts the force–time function can be approximated using:

$$f(t) \cong H \cdot \left(\frac{4}{3}\right) \cdot R^{1/2} \cdot \varepsilon^{*} \cdot d^{3/2} \tag{4}$$

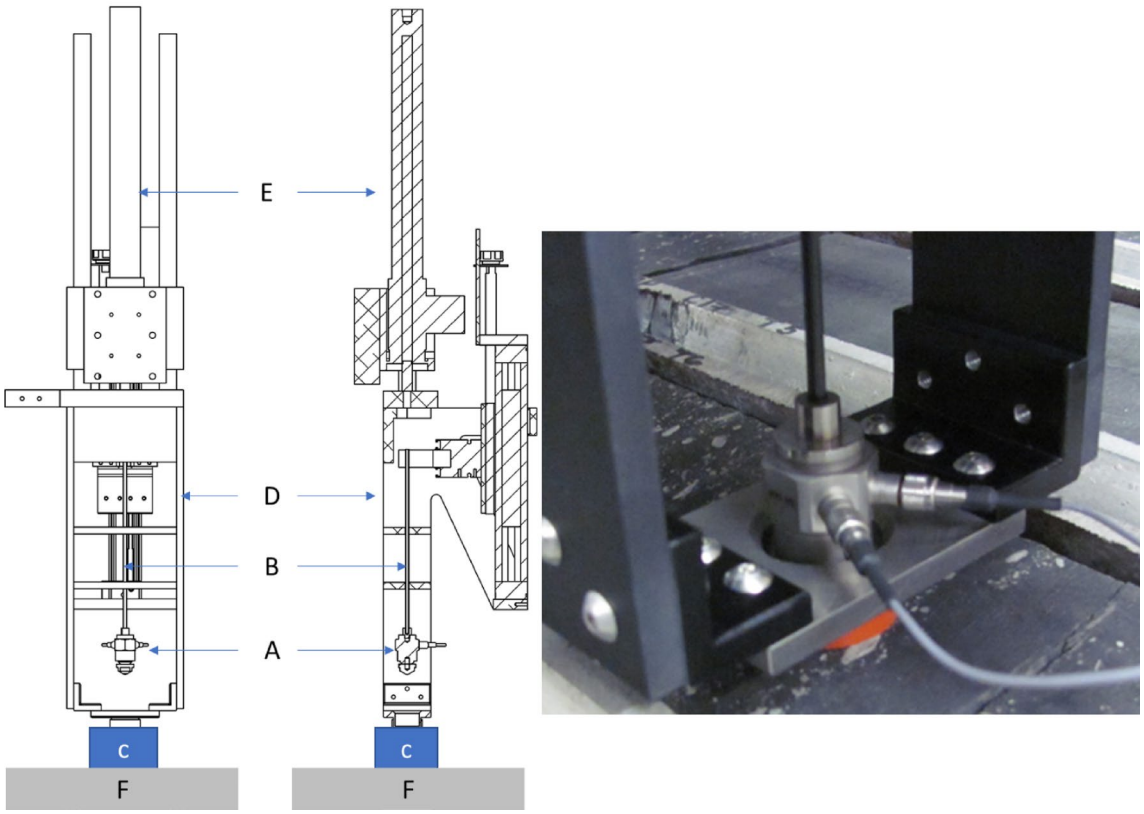

Fig. 2 Schematic diagram of the testing apparatus where an instrumented impactor **A** suspended on a carbon fiber rod **B** is dropped onto a sample surface **C** while recording high resolution force and acceleration. The frame **D** holding the impactor is forced against the sample by a pneumatic ram **E** to immobilize the sample against the table **F** allowing the sample to be modeled as if it has infinite mass. A photograph on the right side of the figure shows the impactor

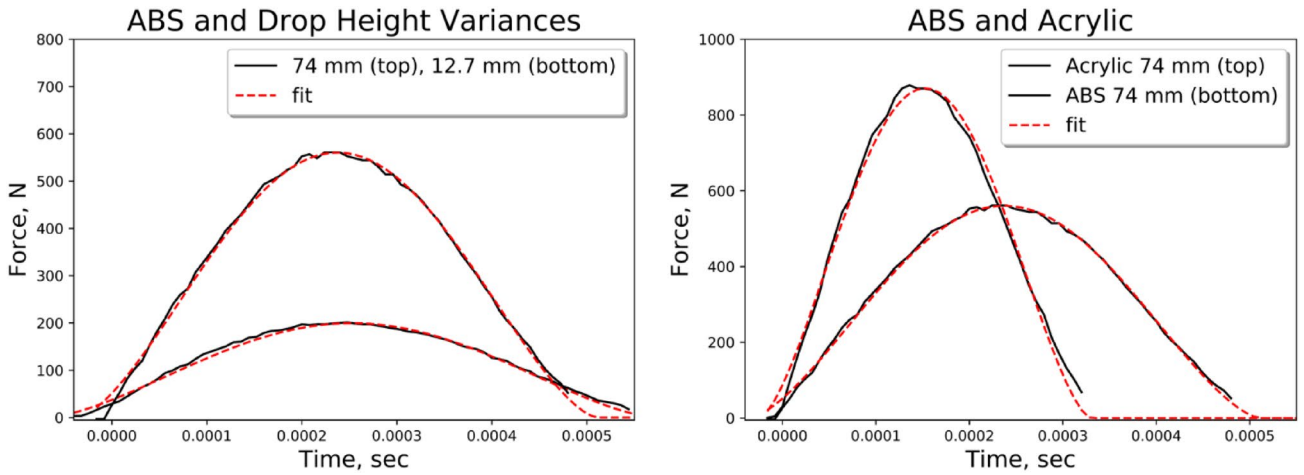

Fig. 3 Left: force–time curves for two impacts at 12.7 mm and 74 mm drop heights on ABS plastic (black) and Hertzian solution fit (red dashed). Right: force–time curves for two materials (ABS and Acrylic) at 74 mm drop height (color figure online)

$$d \cong sin\left(\frac{\pi\left(t-t_0\right)}{2T^*}\right)\cdot d_{max} \tag{5}$$

where, d is the displacement, R is the tip radius, t is the recorded time, t_0 is the time of impact, T^* is the half-time of impact ($^{2.94\cdot d_{max}}/_{2\,.\,V}$), and d_{max} is the maximum displacement. The parameter H was introduced by Gramin et al. (2016) as a dimensionless hardness parameter which for the case of ideal elastic impact has a value of unity.

The maximum displacement can be described as:

$$d_{max} = \left(\frac{15\cdot M\cdot V^2}{16\cdot R^{1}/_{2}\cdot \varepsilon^*}\right)^{2/5} \tag{6}$$

where, $M = \left[\frac{1}{M_i}+\frac{1}{M_s}\right]^{-1}$ and V are the effective mass and velocity of the impactor, respectively. R is the tip radius, and ε^* is the effective stiffness of the contact. M_i and M_s are the mass of the impactor and the sample, respectively. The relationship between the effective contact stiffness and the reduced Young's modulus of the sample (E^*) is provided below:

$$\frac{1}{\varepsilon^*} = \frac{\left(1-\nu_{tip}^2\right)}{E_{tip}} + \frac{1}{E^*} \tag{7}$$

where, ν_{tip} is the Poisson's ratio of the indenter tip material, and E_{tip} is the Young's modulus of the indenter tip material. For a practical case when $M_s \gg M_i$, then $M \cong M_i$. If the sample is linear elastic and isotropic, $E^* = \frac{E}{(1-\nu^2)}$, where E and ν are the Young's modulus and Poisson's ratio of the test sample.

We note that the equations in (2, 3, 4) and (5) can be written generically as:

$$f = A\cdot\left(\sin\left[\frac{\pi\cdot\left(t-t_0\right)}{B}\right]\right)^{3/2} \tag{8}$$

Thus, fitting the data to the model involves the determination of three parameters: A, B, and t_0. In terms of A and B, Eqs. (2–5), and (8) can be written as:

$$A = \left(\frac{4}{3}\right)\cdot\left(\frac{15}{16}\right)^{3/5}\cdot HM^{3/5}\cdot V^{6/5}\cdot R^{1/5}\cdot {\varepsilon^*}^{2/5} \tag{9}$$

$$B = 2.94\cdot\left(\frac{15}{16}\right)^{2/5}\cdot M^{2/5}\cdot V^{-1/5}\cdot R^{-1/5}\cdot {\varepsilon^*}^{-2/5} \tag{10}$$

Combining Eqs. (9) and (10), we note that:

$$A\cdot B = 3.625\cdot H\cdot M\cdot V \tag{11}$$

Considering E_{tip}, ν_{tip}, and R as known a priori, from measurements of A and B, one can determine any pair of parameters H, E^*, M, and V provided the other two parameters are treated as known. It is worth noting a few general observations, limitations, and potential applications that result from these relationships:

(1) Assuming M and V are known, E^* can be determined from the measurement of the duration of impact (B) without any knowledge of the amplitude (A). This allows for potential application of the impulse hammer method using a qualitative force sensor simply by measuring the time of impact.
(2) If the force measurement is quantitative but its exact calibration is not well known, using H as a free parameter in the analysis of an elastic impact allows for determination of the force calibration even for the case that E^* is not known. This provides a means to calibrate a force sensor operationally.
(3) If the force calibration is well constrained, then E^* can be determined even for cases where either M or V are unknown by simultaneously solving for the additional unknown.
(4) The product $A\cdot B$ is a simple linear function of the momentum of the impactor at the time of impact and is independent of R. of the impactor and E^* of the sample.
(5) If the impact is elastic, the uncertainty in E^* is proportional to the uncertainty in $\sqrt{R}$.

For elastic properties measurements reported in this study we use a spherical tip with a radius $R = 3.81$ mm formed from tungsten carbide. To promote elastic deformation, we use a sensor with small mass (69 g) and drop it from a small drop height (normally 12.7 mm). In our set-up, the sensor is designed to freefall and thus we start by assuming the velocity of impact can be calculated as $V \cong V_f \equiv sqrt(2g\cdot h)$, wre g is the acceleration due to gravy and h is the drop height. The sample is pressed against the table so as to immobilize it. As a result, even though the sample itself may have a mass similar to that of the impactor, the effect of immobilization against the table allows us to assume the sample mass is effectively large with respect to the impactor such that we can assume $M \cong M_i$.

The force versus time function is recorded using a digital oscilloscope and fit to the model via a least squares minimization using Eq. (6) to determine the free parameters A, B, and t_0. To account for potential uncertainties in impact velocity and effective mass, from A and B we then determine three values for E^* that we refer to as E^*_M, E^*_V, and E^*_H, where the subscript denotes the secondary parameter that is treated as uncertain.

Computation of E_M^*.

Assuming $H = 1$ and $V = V_f$, we solve for M. v Eq. (11) and then E_M^* using Eq. (9). This addresses the uncertainty in the assumption that the sample is fully secured to the table. Since in our case the sample is not free to move, we interpret the resulting value of M_s as the "effective" mass of the sample that approximates the effects of a partial recoil of the sample when impact occurs.

Computation of E_V^*.

Assuming $H = 1$ and $M = M_i$, we solve for V using Eq. (11) and then E_V^* using Eq. (9). This accounts for uncertainties in the velocity of impact, accommodating for uncertainties in the drop height or the influence of external forces other than gravity (e.g., forces due to the wires connected to the sensor or friction on the guide rod).

Computation of E_H^*.

Assuming the values of M and V are treated as known, we solve for H using Eq. (11) and then E_H^* using Eq. (9). In this case, H becomes an estimate of the fractional momentum retained by the impactor.

$$H = \frac{A \cdot B}{3.625 \cdot M \cdot V} = \frac{Momentum_{measured}}{Momentum_{assumed}} \tag{12}$$

It should be noted that if the force calibration is uncertain, the uncertainty also contributes directly to the inferred value of H as an additive term. In this case, the term H becomes a qualitative index related to momentum transfer. Assuming the force calibration is known, and M and V are well constrained, the value of H allows for a first order compensation for inelastic processes or energy that leaves the system due to dynamic processes such as elastic wave propagation. It is noted that the lower the value of H, the less appropriate the elastic model is for analysis of the elastic stiffness of the sample.

Relationships between E_M^*, E_V^*, and E_H^*.

It can be shown that for $H < 1$, $E_M^* \leq E_H^* \leq E_V^*$. It is also interesting to note that for a given force versus time curve, the best fit of Eq. (8) results in $H|_{V=V_f,M=M_i} = {}^{V}/_{V_f}|_{H=1,M=M_i} = {}^{M}/_{M_i}|_{H=1,V=V_f}$. As a result, from A, B, and H, one can compute E_M^*, E_V^*, *and* E_H^*.

4 Experimental Data

4.1 Elastic Analysis on Reference Materials

The primary data set that was acquired for this study is composed of a variety of materials including a series of plastics covering a range of properties at relatively low stiffnesses, a common ceramic (Macor) providing a strong elastic material with high stiffness, and two rock samples to demonstrate application to characterization of natural heterogeneous materials. The plastics and Macor were picked for their homogeneity, hence allowing for a more robust comparison between the two types of processing. The plastics included ABS, Acrylic, Nylon, PETG, Polyester, Polystyrene, Polysulfone, and Ultem.

The study started by testing each of the samples using the spherical tip. Multiple measurements were made on each material along linear profiles with individual measurements spaced by ≥ 4 mm so as to avoid being influenced by previous measurements. Figure 3 shows data from two impacts on ABS plastic at 12.7 mm and 74 mm drop heights and elastic stiffness differences between two materials (ABS and Acrylic) at 74 mm drop height. The black curves are the measured force–time functions, while the red dashed lines represent the computed force–time curves that best fit the measured data. Excellent fits to the elastic contact model are observed in these measurements. An overview plot comparing results from all materials and drop heights together is shown in Fig. 4. Overall, the dataset exhibits the expected trends illustrating the validity of the measurement approach over a wide range of materials and stiffnesses. Comparisons of E_H^* for the plastics and Macor at 12.7 mm drop height versus values expected based on independent measurements using a combination of ultrasonic velocities, densities, and published flexural rigidities show good correlation providing justification for the assumption $M \cong M_i$ and use of E_H^* as the default interpretation. The values of E_M^* and E_V^* plotted a function of E_H^* illustrate the strong correlations between the three E^* values and relatively small spread between the different estimates suggesting the use of E_H^* as the default interpretation. The wider range in values observed for the shale and Wonder Stone reflect sample heterogeneity that correlates with bedding, while the range in values in the plastics are dominated by systematic variations associated with drop height and reduction in H, suggesting non-linearities in material response.

4.2 Force vs. Displacement Transformation for Enhanced Analysis

The analysis above is only strictly valid for the case of elastic impact. However, the patterns and trends in the data with regard to the compensation parameter H as a function of drop height and material are suggestive that the deviations from elastic theory are capturing valuable information about variations in inelastic properties.

With the desire to extend the application of this measurement technique to studies of both elastic and inelastic properties, we note that if force, velocity, and mass are well calibrated and in the absence of external forces other than gravity, we can integrate the force with respect to time twice to compute the displacement versus time. As a result, we

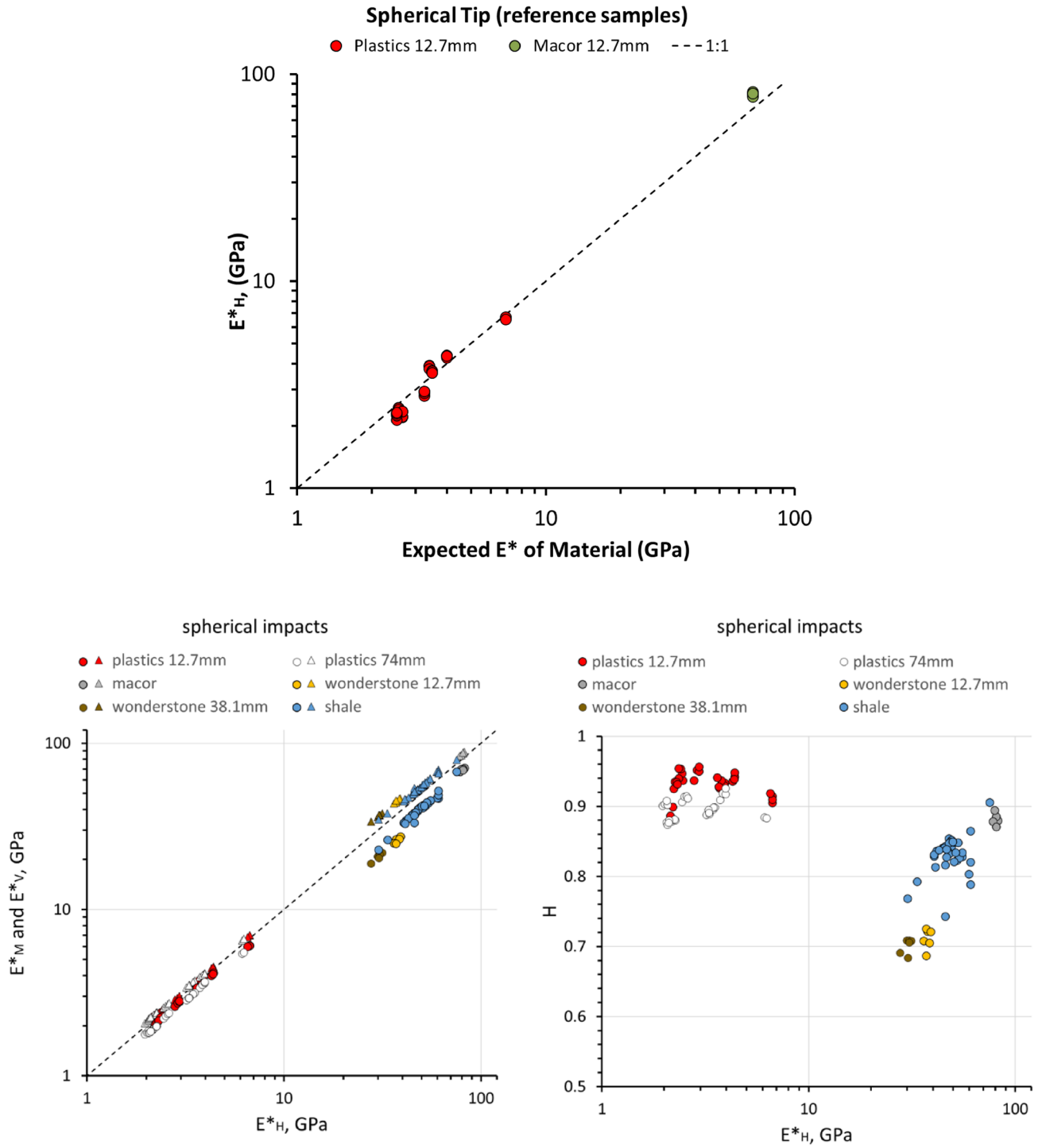

Fig. 4 Overview of results from measurements using a spherical tip with $R = 3.81$ mm. In the top graph, the results of E_H^* versus expected values of E^* from independent measurements of elastic constants of the homogeneous reference materials illustrates good agreement. In the lower left graph, E_M^* (circles) and E_V^* (triangles) are plotted versus E_H^*. While for the two rocks (shale and Wonder Stone) the ratio E_V^*/E_M^* approaches a factor of two, the different estimates of E^* remain strongly correlated. On the lower right, a cross plot of H versus E_H^* illustrates that plastics and macor exhibit the highest H values indicating they exhibit the most elastic response, while the Wonder Stone shows the largest deviations from elastic theory

obtain a measure of the force versus displacement during the impact.

In the analysis that follows, we show how the force–time curves can be analyzed quantitatively in the context of traditional indentation theory, resulting in additional physical constraints on the inelastic processes occurring during dynamic impact. To do this, we assume that the impactor can be approximated as a rigid body acted upon by a constant force (e.g., gravity) and the measured force of impact. We then convert the measured force–time curves to force–displacement via double integration as a function of time using Newton's laws of motion and assuming that the initial velocity is calibrated at the time of impact to determine the first constant of integration. The integration of the force–time curve requires that the time of impact (t_0) is known, which can be extracted via a waveform arrival picking technique, e.g., thresholding or Akaike's Information Criterion (AIC) on the measured force–time curves and/or the measured acceleration-time curves. Beginning at t_0, an acceleration curve is calculated using $Force = mass \cdot acceleration$. This calculated acceleration curve can then be converted to an incremental change in velocity curve (referred to here as vel_delta) by multiplying the acceleration by the timestep length. Once the vel_delta curve is obtained, the free fall velocity can be assigned to the identified impact time (t_0). The free fall velocity can then be modified at each subsequent timestep by the corresponding vel_delta increment, thereby creating a velocity–time curve. Incremental displacements (at each timestep) are then calculated by multiplying the calculated velocity–time curve by the timestep length. A total displacement–time curve is then just the incremental summation of subsequent displacement increments from each timestep.

Figure 5 (left) provides an example of the transformation for the ABS data already shown in Fig. 3. The top figure recalls the measured force–time functions (black lines) and the purely elastic Hertzian fits (red dashed lines). The resulting computed force–displacement curves are shown in the bottom figure. It is apparent that these measurements are elastic because (1) excellent fits to the Hertzian model are seen in the top figure, and (2) the loading and unloading slopes are nearly identical while also having negligible net displacement (h_f or h_r).

The value of the data analysis method for the case of an elastic impact is in calibration of the constant of integration for velocities (e.g., to confirm or determine the impact velocity for a given experimental configuration). Once validated, the method can be used to extract information regarding inelastic impact and damage to the material being tested.

All the measurements performed with the spherical indenter tip were also conducted with a cube corner tip, which was seen as more likely to impart substantial inelastic deformation. Figure 5 (right) shows the results obtained with the cube corner tip on ABS plastic. In this case, a measurable and readily observable, inelastic deformation occurs resulting in notable net displacements. The force–time functions in the top plot appear to be distorted and no longer represent mirror images across the maximum force as was observed for elastic impact. Red points indicate t_0, while magenta points indicate the "omes zero does not necessarily take place at the timestep of maximum force. When inelastic deformation is present, the timestep where velocity becomes zero occurs measurably post-maximum force. One can conceptualize this as an indenter tip reaching maximum force while still extending into the sample as the sample deforms and eventually reaching a point of zero velocity prior to "bouncing" back.

Figure 5 (right bottom) also shows the computed force–displacement curves for the cube corner impacts along with several key parameters, such as turn-around point (magenta), impact point (red), unloading regression end point (cyan box), loading regression start point (red box), x-intercept of the unloading stiffness curve (black box with red outline), and h_c (yellow box with black outline). The loading regression start point references turnaround point," where computed velocity becomes zero. It is worth noting that when inelastic deformation is present, the time in which velocity becthe point in which the most linear region exists between it and the turn-around point to be used for linear regression and loading modulus determination. The unloading regression end point refers to the ending data point where the most linear region of the unloading curve (tied to the turn-around point) exists for determining the unloading stiffness. Unloading stiffness curves are shown in the figure as dotted lines. An initial observation of these three measurements of differing drop heights shows that the loading and unloading stiffnesses are not observed to change as a function of drop height; meaning that for these variances in inelastic deformation, repeatable measures of reduced Young's modulus are possible and are not a function of drop height because the initial stage of the unloading curve is largely free of inelastic deformation. It also emphasizes that at these drop heights, the magnitude of inelastic deformation follows the same loading stiffness slope meaning that these drop heights do not fundamentally alter the physical response as a function of inelastic deformation. Similar results were observed in the results from the other plastics.

Representative measurements on rock samples are shown in Fig. 6. The spherical and cube corner impacts were performed at the same depth locations, only a few millimeters apart in the horizontal direction so that measurements from individual depths can be compared in both the elastic and inelastic space. The core material exhibited multiple scales of heterogeneity and anisotropy but exhibited strong vertical transverse isotropy allowing measurements of similar depths to be made in the same depositional layer. Initial

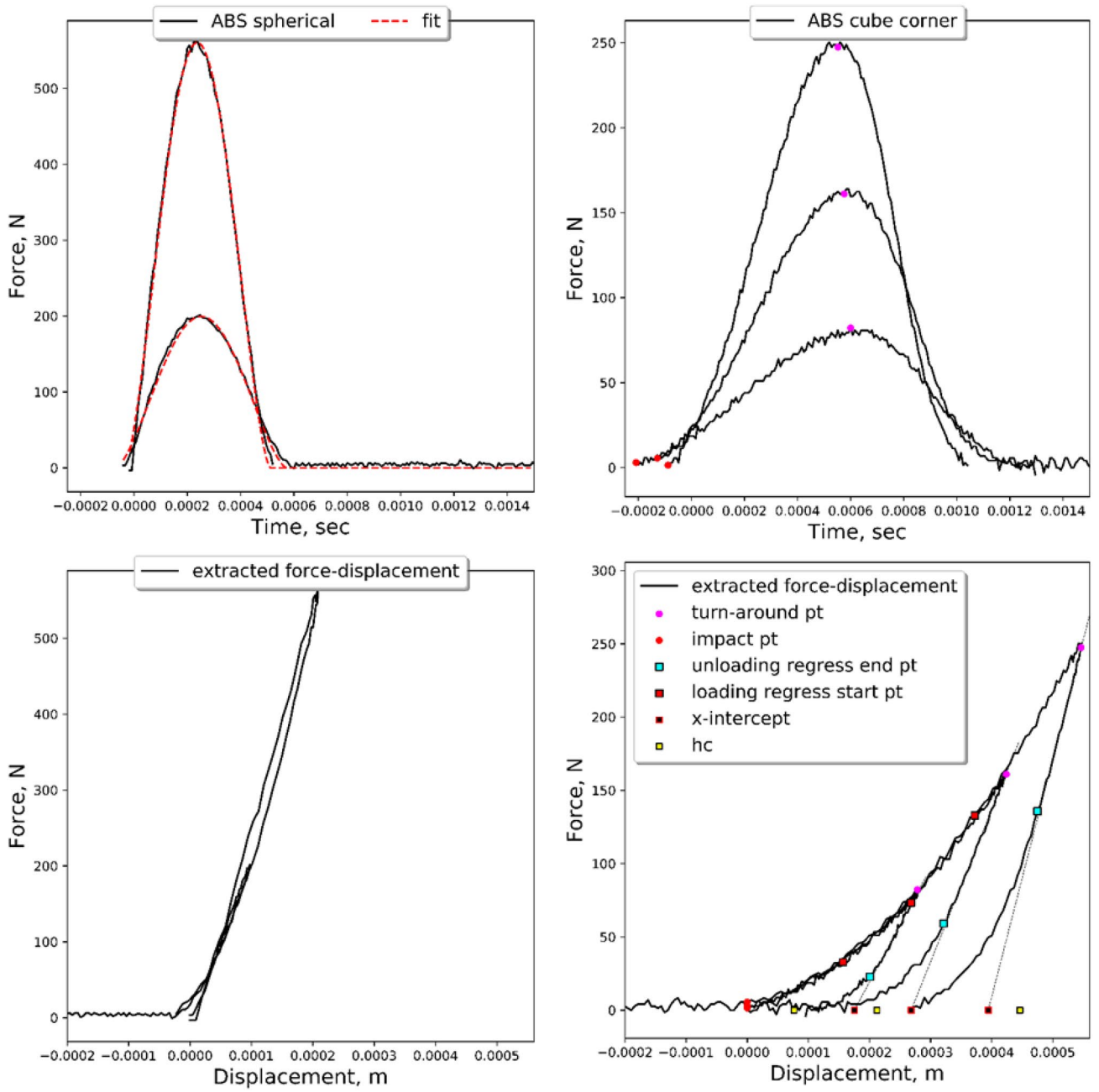

Fig. 5 Left: measured force–time and computed force–displacement curves for spherical impacts on ABS plastic at two different drop heights (12.7 mm and 74 mm). Right: measured force–time and extracted force–displacement curves for cube corner impacts on ABS plastic at three drop heights (12.7, 38, and 74 mm)

observations of these force–time functions show that a variety of materials (i.e., mechanical properties) and response types (brittle versus ductile) are present. Figure 6 (left column) displays a subset of the spherical impacts along with the Hertzian contact fits. Good fits to the Hertzian model are observed, while also showing that some inelastic deformation was present (i.e., visible differences in curve shape and residual deformation). Using these spherical force–time functions, force–displacement curves are computed to obtain information on the loading and unloading (reduced Young's modulus) moduli. The bottom-left of Fig. 6 shows the extracted parameters, including h_c. The right column of Fig. 6 show the cube corner results for the same depths as probed by the spherical indenter shown in the left column. Cube corner responses from measurements on the rock samples were more complex. Notable oscillations in the force–time function are commonly observed in the cube corner measurements on rocks. These are likely due to the

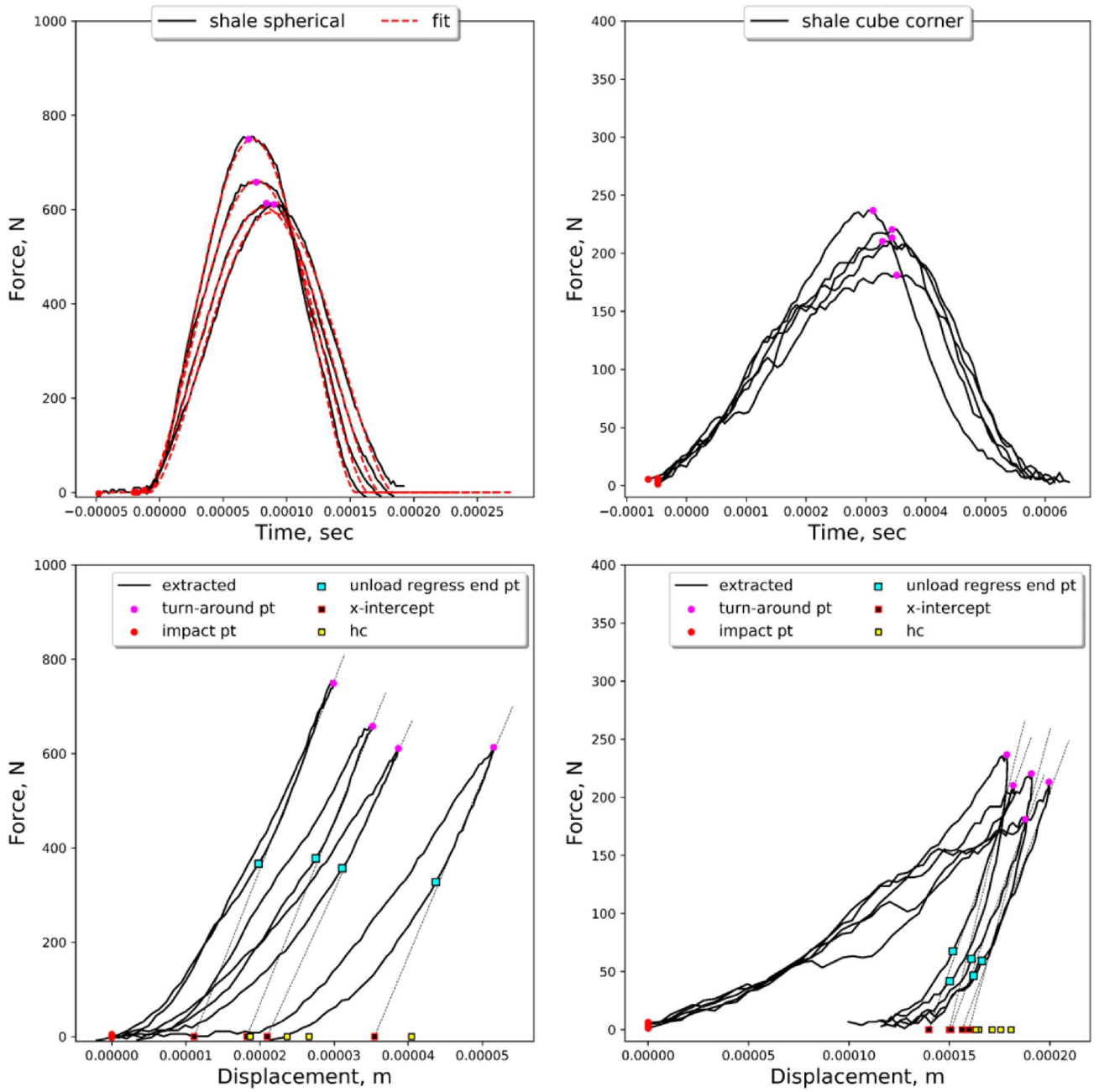

Fig. 6 Force–time and force–displacement curves for shale with spherical (left column) and cube corner (right column) tip geometries

brittle nature in which the rock deforms and are likely exaggerated by ultrasonic reverberations in the force transducer excited by the brittle failure. This interpretation is supported by observations of disaggregated material pushed up by the indentation process. Though the curves measured on rocks do not appear as ideal as those in more plastic materials, the reproducibility in response demonstrates that the extraction of meaningful force–displacement curves and associated parameters are still possible despite more noise in the computations.

4.3 Validation of the Force vs. Displacement Transformation

The computed force displacement curves were validated by imaging the indentations. Figure 7 is an image of one of the plastic samples interrogated with various indenter tip geometries and drop heights. Labels of spherical, cube corner, and drop height differences are shown. From this image, additional indentations caused by bounces of the impactor can also be seen. Using standard microscopy techniques, the

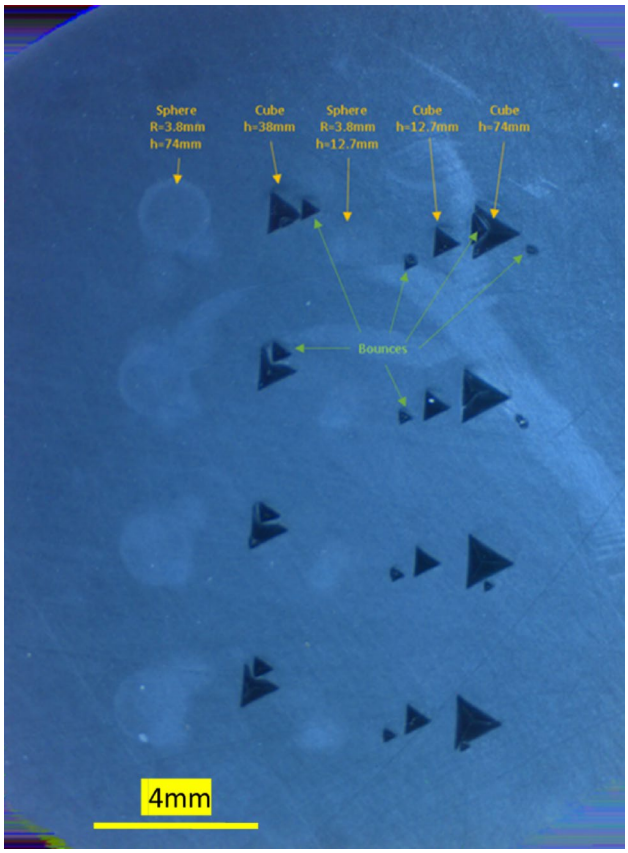

Fig. 7 Plastic sample showing spherical and cube corner impact final displacements for several drop heights. Bounces are clearly visible. Spherical impacts also show very minimal permanent displacement

extraction of the geometry of indentation is readily determined for all the plastic samples, along with several of the other material types. The extracted final depth (h_f) can be determined using measurements of the side length and the geometric relationship between side length and depth of a cube corner. Figure 8 shows white light interferometry images of a cube corner impacts on a shale sample providing a detailed height map of the indentations at several locations. This image clearly shows the permanent indent geometry, while also showing distinct features of inelastic deformation and pile-up. Images for several shale samples using interferometry techniques were performed to validate a broad range of impact craters associated with a variety of mechanical responses (i.e., rock types). Again, the shale specimens were sawcut and the quantified surface roughness is shown in Fig. 8, where the magnitude of roughness is on the order of a few microns, which is significantly smaller than the pile-up and final indentation depths measured (h_f).

Figure 9 shows the results of the imaged widths converted to depth (via geometrical relationships associated with the shape of indentation or the direct extraction of depth via interferometry data). These are plotted against h_f (determined from force–displacement analysis), where very good agreement is seen.

4.4 Elastic Stiffnesses and Fractional Energy Loss

Figure 10 shows comparisons of various computed parameters for spherical impacts. E^*_{ul} here refers to the traditional indentation theory derived reduced Young's modulus from Eq. (2–4), which uses the unloading portion of the force–displacement curve. E^*_L here refers to the loading "modulus" from the force–displacement curves. We note that the loading and unloading moduli from the force displacement processing correlate well. E^*_{ul} and E^*_L are observed to bracket the values of E^*_H determined using force–time analysis, consistent with the fact that the force–time processing is based on a fit to the entire curve. This illustrates how even in the case of the spherical tip, the force–displacement analysis can be used to extract second order responses relating to inelastic processes, the force–time analysis can be used as a simple method to extract an average stiffness.

While a single measurement can be used to characterize mechanical properties at a particular location in a sample, it is instructive to compare elastic stiffnesses using multiple measurements on a given material with varying drop heights and tip geometries. Figure 11 compares E^*_{ul} from the cube corner and the spherical indents on the same materials. Here, we observe a reduction in the modulus for measurements acquired on cube corner impacts. For the plastics, the shift in E^*_{ul} values between cube corner and spherical indents are relatively small and consistent in magnitude scale independent of stiffness as might be expected for a plastically deforming material. The shift in values observed in the plastics is not understood at this time but may reflect limitations of the assumptions for determination of E^*_{ul} for the cube corner for the case of dynamic macro-indentation. In contrast, the reduction in E^*_{ul} via cube corner as compared to spherical impacts for shale and Wonder Stone is considerably larger and does not correlate with stiffness variations. A working hypothesis is that the large reduction in apparent stiffness between the two tip geometries in the case of the rocks reflects the softening effects of brittle damage during cube corner indentation in these two materials. This contrasting behavior between the plastics and the rocks offers a potential application directed at quantifying the strength and brittleness of a material through combined interpretation of spherical and cube corner measurements.

Fractional energy loss can also be readily determined from the force–displacement analysis by integrating force with respect to displacement and dividing by the kinetic energy at impact. This is plotted in Fig. 12 against H determined by the force–time processing. The strong correlation over a wide range of materials, stiffnesses, and drop heights confirms the physical interpretation for H related

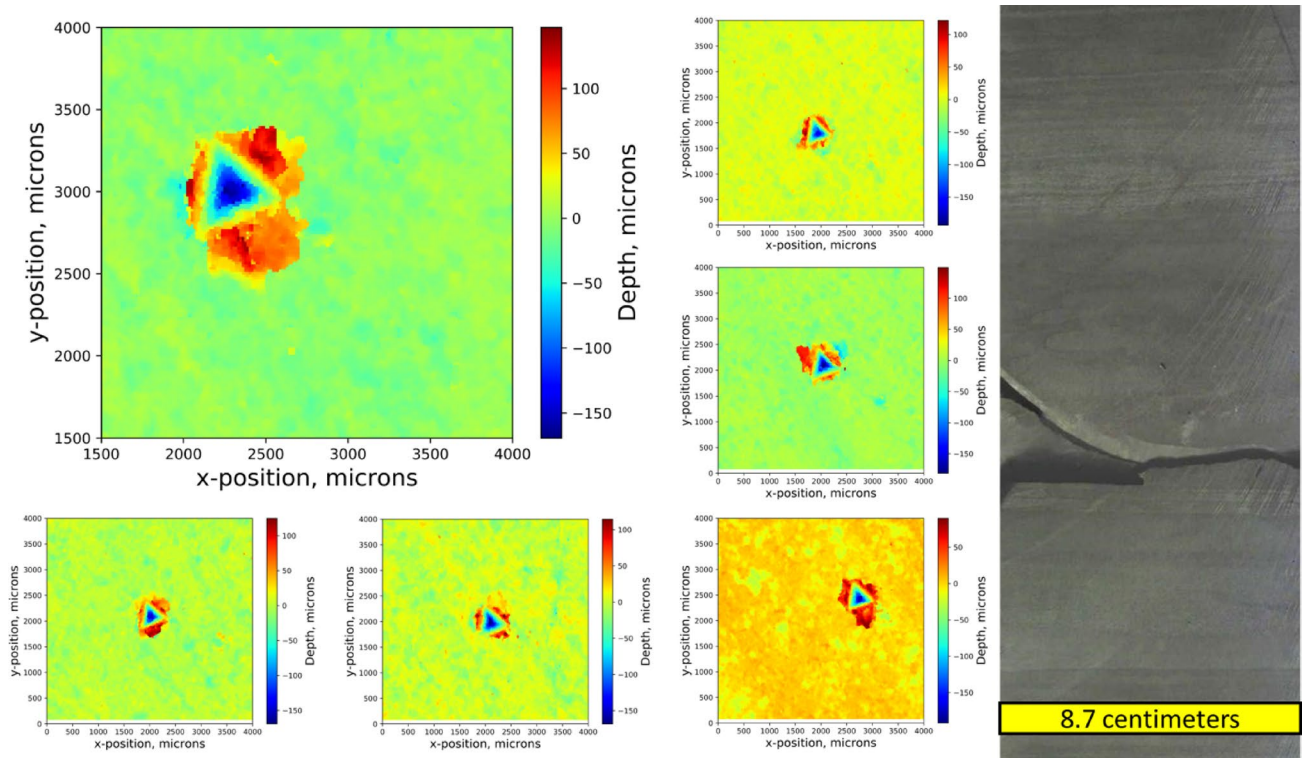

Fig. 8 Interferometry results for several cube corner impacts on a shale sample. Geometry of the impacts and pile-up are clearly identified. A photograph of the shale sample is shown on the right

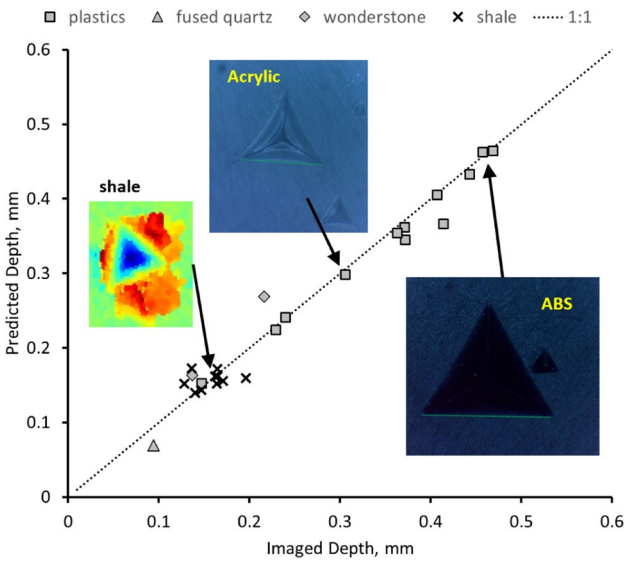

Fig. 9 Comparison of final depth (h_f) extracted from force–displacement analysis with that of image results (h_f) of the indentation post-test. Excellent agreement between extracted displacement data and the actual imaged depths is shown

to Eq. 10even in cases of significant energy loss through inelastic processes.

5 Discussion

The new dynamic indentation tool that is described this study was initially designed as a nondestructive evaluation device meant to rapidly probe elastic stiffness at a vastly increased spatial resolution compared to traditional static or dynamic elastic testing. As such, the system provides a robust output in the form of a reduced Young's modulus whereby both the acquisition and interpretation are well supported by contact mechanics theory in the case of a spherical tip geometry. As an illustrative example, Fig. 13 provides an output map obtained on a section of asphalt along with a photograph and a gas permeability data set obtained at the same locations. The mechanical measurement output consists of the reduced Young's modulus E^* as well as the H parameter introduced in Sect. 3, and which was shown in Fig. 13 to be strongly negatively correlated with the amount energy dissipated throughout the impact process.

A rapid observation of Fig. 13 attests to the high contrasts in physical properties that can be observed among the asphalt components but also to the spatial coherence among these properties and the opportunity to derive functional

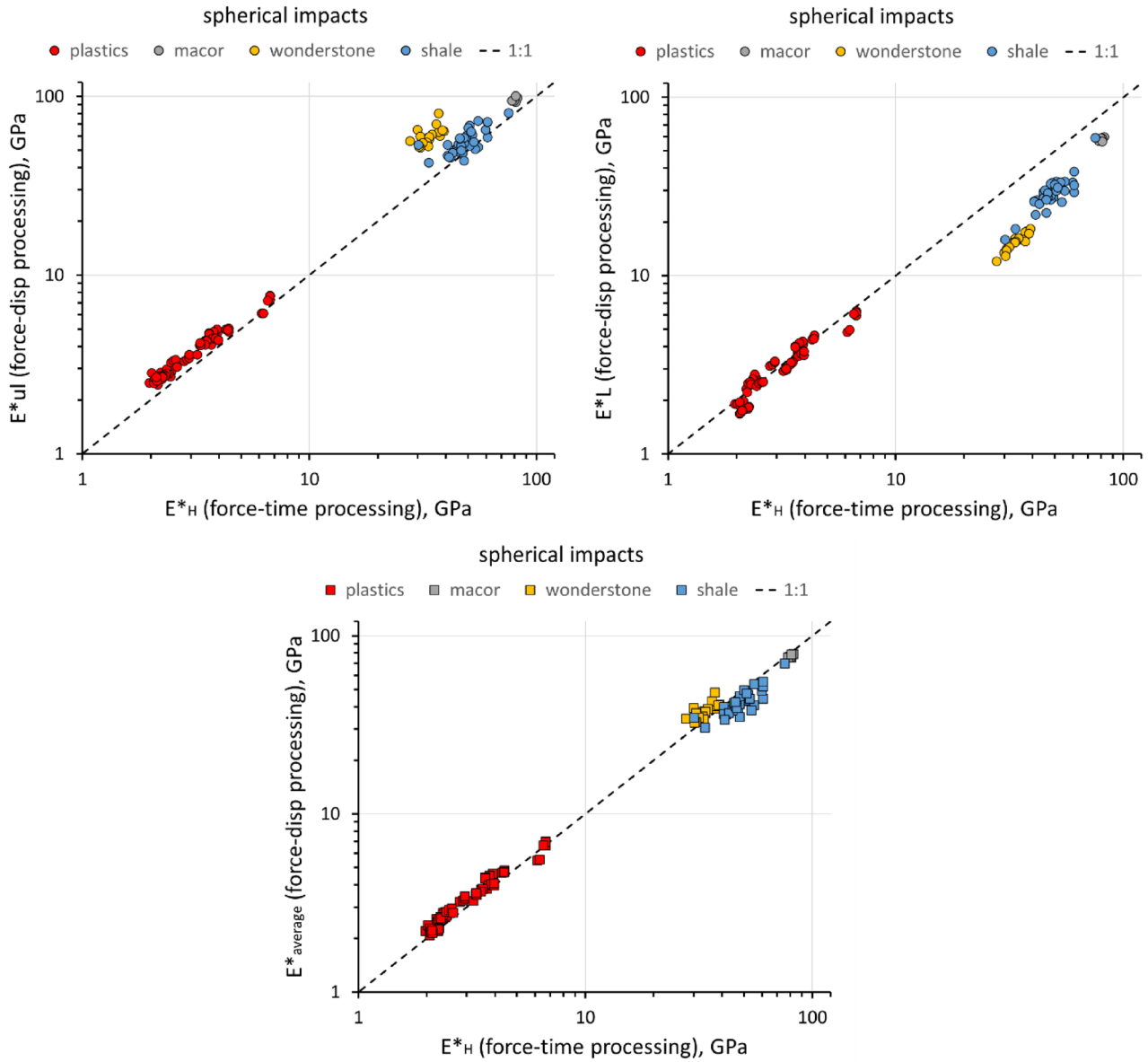

Fig. 10 Comparisons of E^*_{ul}, E^*_L, and their averages from force–displacement analysis with E^*_H from force–time analysis for all the spherical tip measurements. The force–time analysis compares most favorably with the average of the loading and unloading moduli, consistent with the force time analysis operating on the entire force time curve

relationships based on point-wise correspondences. Focusing on E^* and H, the maps indicate in this particular case that the stiffer domains associated with rock aggregate tend to also be much less dissipative than the softer domains dominated by the asphalt binder. More thorough examination might allow to mechanically classify different components or mechanical condition of binder and aggregate in a particular sample and ultimately formulate predictions as to the macroscopic behavior of the entire section.

Guided by the well-established static indentation technique and based on the fact that the force vs. time data suggested more could be learnt regarding the mechanical properties being probed, a transform from force vs. time to force vs. displacement was devised, which allowed recasting the interpretation framework into the existing framework of static indentation and hence explores further the tool/material interaction. The comparison between stiffness values derived from both methods using the same raw data showed overall consistency. Moreover, the use of a cube corner indenter verified the validity of the displacement calculation based on the dynamic test. Hence the investigation of the use of the static indentation framework helped confirm and extend the initial interpretation workflow.

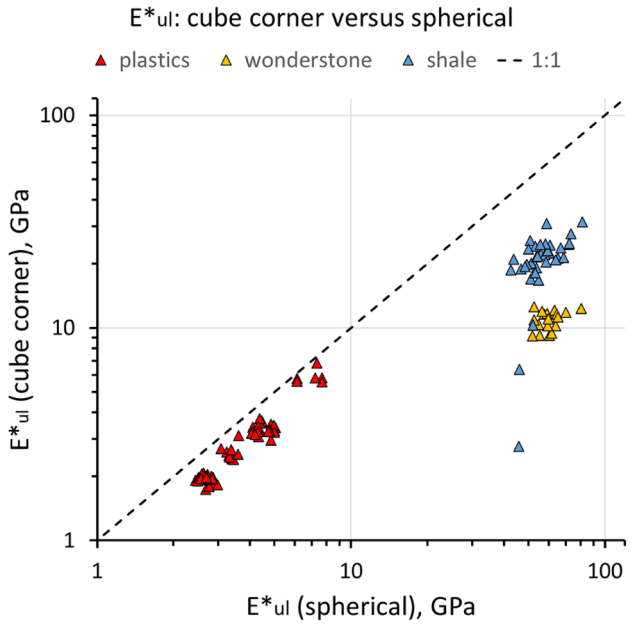

Fig. 11 Comparison of E^*_{ul} from cube corner impacts with the corresponding values from the measurements using the spherical tip. The spherical tip is always observed to yield higher values of E^* than the cube corner. For the shale and Wonder Stone (blue and yellow) this likely reflects the softening effects of damage in the case of the cube corner impacts. The physical reasons for the systematic shift in values for the plastics (red) is not known (color figure online)

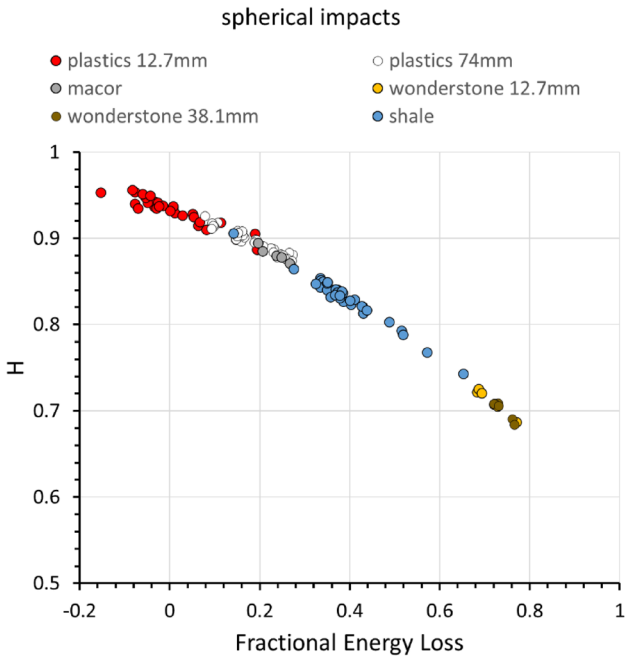

Fig. 12 H from force–time analysis versus Fractional energy loss computed from force–displacement analysis for all measurements using the spherical tip. The tight relationship that is independent of the drop height and material illustrates that for the case where mass and velocity are known, H can be interpretated as an energy dissipation term. The small negative values of fractional energy loss in some of the plastics at 12.7 mm drop height is thought to reflect the effects of uncertainty in the time of impact for cases where the force–time function is emergent at the scale of noise in the force measurement itself

Though the extraction of several independent metrics tied to material mechanical properties is made possible by this analysis and ultimately enhances the characterization output in terms of profiling and mapping, some uncertainties were also identified which should be addressed in further studies. The comparison between the results obtained using spherical and cube corner indenters (Fig. 11) showed that there was likely to be value in combining the two based on the fact that the cube corner is expected to induce some amount of damage in brittle materials, which can be used as an indication of mode of deformation and proneness to fracturing. In the case of non-brittle materials such as plastics however, a match should be expected when using either of the indenters. As was pointed out earlier, there are inherent difficulties in accurately predicting the surface function in the interaction between a material and a given indenter and moderate discrepancies should be accounted for when reasoning in that space. Regarding the dynamic indentation process more specifically, one may question whether the calculated elastic modulus better reflects the dynamic or the static one. Considering the continuous loss of kinetic energy during the indenter/material interaction and the constant change in effective contacting surface area, there is no set strain rate throughout the test. Instead, it varies from very high at the contact initiation to transiently low at the time the maximum force is reached. Additional factors such as boundary conditions and the presence of fluids might have a greater influence in the result and such assessment should rather be made on a case-by-case basis. Finally, an important aspect that also deserves further investigation, both from a technique and application point of view, is the effect of using a cube corner in terms of brittle damage. In Fig. 11, it can be safely assumed that the reason for the substantially low stiffness seen when using the cube corner as opposed to the spherical indenter is due to the fact that in the case of the cube corner, the material that was unloaded had sustained a certain amount of cracking-related inelastic damage caused by the indenter shape. More work should be carried out to first verify what type of damage is imparted by the indenter, then establish whether this can be used as an indicator of strength degradation (i.e., ductile and brittle behavior) which could find direct applications in subsurface exploitation.

6 Conclusion

This paper reviews traditional static indentation and dynamic impact testing for elastic properties measurements. A dynamic impact method is used to determine both

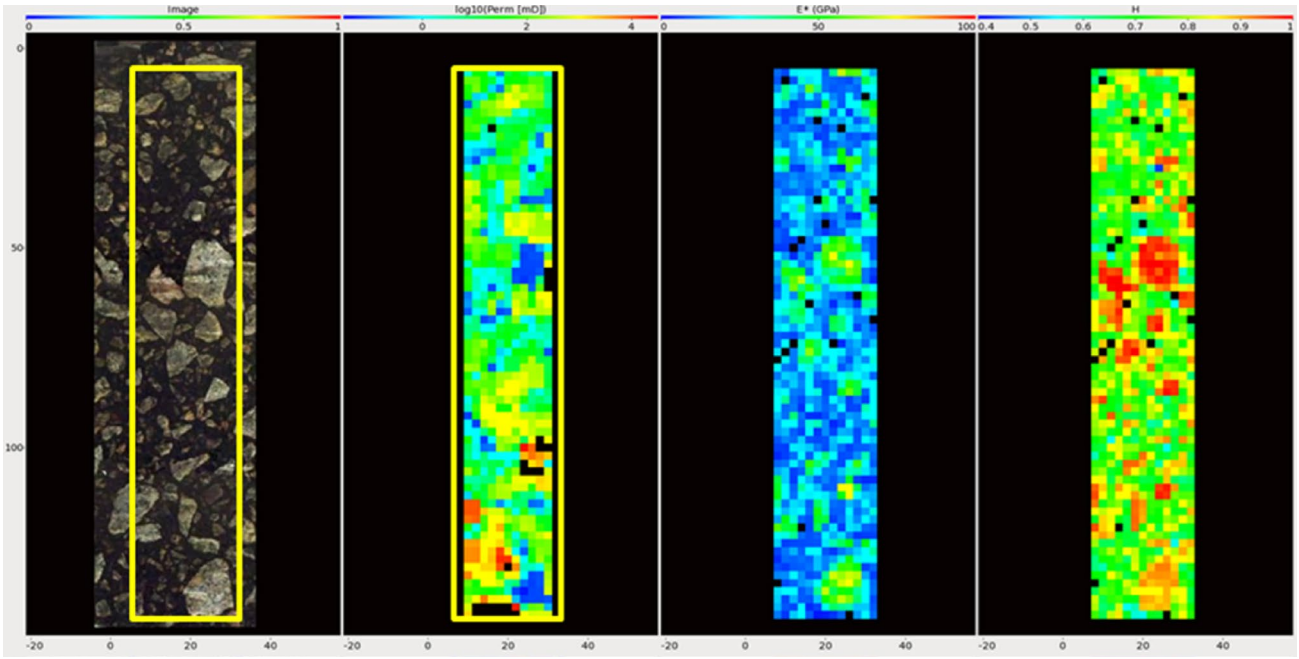

Fig. 13 Example of a physical properties mapping result for a section of asphalt comprising a photograph, a probe permeability map, and a map of the reduced Young's modulus E^* as well as its energy loss parameter H. Measurements were made on a 2-mm grid spacing. X–Y scales in the figure are in mm

mechanical properties and failure properties for a variety of materials where the testing setup can be adjusted to induce variable amounts of elastic as well as inelastic responses. Several key conclusions are summarized below:

- This paper describes a method that offers to combine the advantages of a virtually non-destructive mechanical testing framework (indentation theory) with a fast data collection workflow (the dynamic impact) suitable for automated interpretation without the need for direct measurement of displacement or the post-test imaging of indentations.
- Force–time curves can readily be measured on dynamic impacts in a repeatable and predictable manner. The experimental setup is relatively easy to modify such that elastic or inelastic responses can be targeted depending on the specimen's physical properties by controlling the drop height, tip geometry, indenter mass, and impact velocity.
- Force–displacement curves can be extracted from the measured force–time curves without any direct measurement of displacement. This is validated through imaged geometries of the resulting impacts.
- Using force–displacement analysis allows for the interpretation of inelastic physical properties. The results suggest a possible workflow combining spherical and cube corner measurements where comparisons can be made in the context of brittle versus ductile responses.
- The combination of force–time and force–displacement analysis and validation efforts across a wide spectrum of materials allows for the routine application of this technique to be scaled up for rapid assessment of mechanical and failure properties when many thousands of data points are required (e.g., in cases of oil and gas subsurface characterization of fine-scale mechanical variability).

We anticipate that there is much to learn from the comparison between the effects of different indenter geometries. The data have shown that we not only evidence the presence of inelastic processes but that we might also become able to distinguish between hardening through pore collapse and softening through local fracturing, with direct operational implications. The technique allows to generate data sets that would be otherwise very difficult and time consuming to obtain using traditional testing methods and simply offers a unique picture of material heterogeneity, which can be readily incorporated into upscaling workflows.

References

Abid M, Geng J (2020) Effective attributes quantification to bridge gap between elastic properties and reservoir parameters in self-resource rocks. Sci Rep 10(1):1–14. https://doi.org/10.1038/s41598-020-59311-w

Bayuk Irina O, Ammerman Mike, Chesnokov Evgeni M (2008) Upscaling of elastic properties of anisotropic sedimentary rocks. Geophys J. https://doi.org/10.1111/j.1365-246X.2007.03645.x

Boitnott GN, Bussod GYA, McLure J (2014) Automatic Impulse Hammer for Characterization of Mechanical Properties of a Material, United States Patent, Pub. No.: US 2014/0245819 A1

Chang C, Zoback MD, Khaksar A (2006) Empirical relations between rock strength and physical properties in sedimentary rocks. J Pet Sci Eng 51:223–37. https://doi.org/10.1016/j.petrol.2006.01.003

Chen P, Han Q, Ma T, Lin D (2015) The mechanical properties of shale based on micro-indentation test. Pet Explor Dev 42(5):723–732. https://doi.org/10.1016/S1876-3804(15)30069-0

Choens RC, Chester FM (2018) Time-dependent consolidation in porous geomaterials at in Situ conditions of temperature and pressure. J Geophys Res Solid Earth 123(8):6424–6441. https://doi.org/10.1029/2017JB015097

Darrow MS, White WB, Roy R (1969) Micro-indentation hardness variation as a function of composition for polycrystalline solutions in the systems PbS/PbTe, PbSe/PbTe, and PbS/PbSe. J Mater Sci 4(4):313–319. https://doi.org/10.1007/BF00550400

Field JS, Swain MV, Dukino RD (2003) Determination of fracture toughness from the extra penetration produced by indentation-induced pop-in. J Mater Res 18(6):1412–1419. https://doi.org/10.1557/JMR.2003.0194

Fischer-Cripps AC (2007) Introduction to contact mechanics, 2nd edn. Springer, New York

Geng Z, Bonnelye A, Chen M, Jin Y, Dick P, David C, Fang X, Schubnel A (2017) Elastic anisotropy reversal during brittle creep in shale. Geophys Res Lett 44(21):10887–10895. https://doi.org/10.1002/2017GL074555

Gilman JJ (1975) Relationship between impact yield stress and indentation hardness. J Appl Phys 46(4):1435–1436. https://doi.org/10.1063/1.321790

Graham SP, Rouainia M, Aplin AC, Cubillas P, Fender TD, Armitage PJ (2020) Geomechanical characterisation of organic-rich calcareous shale using AFM and nanoindentation. Rock Mech Rock Eng. https://doi.org/10.1007/s00603-020-02261-6

Gramin P, Fisher R, Frooqnia RA, Aiuyb A, Hojnacki P, Boitnott G, Louis L, Hampton J (2016) Evaluation of the impulse hammer technique for core mechanical properties profiling. International Symposium of the Society of Core Analysts, Colorado, pp 21–26

Gutierrez M, Katsuki D, Tutuncu A (2014) Determination of the continuous stress-dependent permeability, compressibility and poroelasticity of shale. Mar Pet Geol. https://doi.org/10.1016/j.marpetgeo.2014.12.002

Hay, Jack C., and G.M. Pharr. 1998. "Exp Investigation of the Sneddon Solution and an Imporved Solution for the Analysis of Nanoindentation Data - Hay_pharr.Pdf." Materials Research Society Symposium Proceedings.

Hertz H (1882) On the contact of elastic solids. J Reine Und Angewandte Mathematik 92:156–171

Hull KL, Abousleiman YN, Han Y, Al-Muntasheri GA, Peter Hosemann S, Parker S, Howard CB (2017) Nanomechanical characterization of the tensile modulus of rupture for Kerogen-Rich shale. SPE J. https://doi.org/10.2118/177628-pa

Johnson KL (1987) Contact mechanics. Cambridge University Press

Keir D, McIntyre B, Hibbert T, Dixon R, Koster K, Mohamed F, Donald A et al (2011) Correcting sonic logs for shale anisotropy: a case study in the forties field. First Break 29(6):81–86

Liu F, Pengcheng Fu, Mellors RJ, Plummer MA, Ali ST, Reinisch EC, Liu Qi, Feigl KL (2018) Inferring geothermal reservoir processes at the raft river geothermal field, Idaho, USA, through modeling InSAR-measured surface deformation. J Geophys Res Solid Earth 123(5):3645–3666. https://doi.org/10.1029/2017JB015223

Louis L, Christian David V, Metz P, Robion B. Menéndez, Kissel C (2005) Microstructural control on the anisotropy of elastic and transport properties in undeformed sandstones. Int J Rock Mech Min Sci 42(7–8):911–23. https://doi.org/10.1016/j.ijrmms.2005.05.004

Louis L, David C, Špaček P, Wong TF, Fortin J, Song SR (2012) Elastic anisotropy of core samples from the Taiwan Chelungpu fault drilling project (TCDP): direct 3-D measurements and weak anisotropy approximations. Geophys J Int 188(1):239–252. https://doi.org/10.1111/j.1365-246X.2011.05247.x

Mazeran PE, Beyaoui M, Bigerelle M, Guigon M (2012) Determination of mechanical properties by nanoindentation in the case of viscous materials. Int J Mater Res 103(6):715–722. https://doi.org/10.3139/146.110687

Oliver WC, Pharr GM (1992) An improved technique for determining hardness and elastic modulus (Young's Modulus). Journal of Materials Research 7(6):1564–83. http://journals.cambridge.org.

Oliver W, Pharr G (2003) Measurement of hardness and elastic modulus by instrumented indentation: advances in understanding and refinements to methodology. J Mater Res 19:2–20

Oyen ML, Cook RF (2009) A practical guide for analysis of nanoindentation data. J Mech Behav Biomed Mater 2(4):396–407. https://doi.org/10.1016/j.jmbbm.2008.10.002

Perrott CM (1977) Elastic-plastic indentation: hardness and fracture. Wear 45(3):293–309. https://doi.org/10.1016/0043-1648(77)90021-7

Pimienta L, Fortin J, Guéguen Y (2015) Bulk modulus dispersion and attenuation in sandstones bulk modulus dispersion and attenuation in sandstones. Geophysics. https://doi.org/10.1190/geo2014-0335.1

Rathbun AP, Carlson SR, Ewy RT, Hagin PN, Bovberg CA, Boitnott GN (2014) Non-Destructive Impulse Based Index Testing of Rock Core. 48th US Rock Mechanics. Geomechanics Symposium held in Minneapolis, MN, USA, 1–4

Reinisch EC, Cardiff M, Feigl KL (2018) Characterizing volumetric strain at brady hot springs, Nevada, USA using geodetic data, numerical models and prior information. Geophys J Int 215(2):1501–1513. https://doi.org/10.1093/GJI/GGY347

Sams Mark S (1995) Attenuation and anisotropy: the effect of extra fine layering. Geophysics 60(6):1646–55

Samuels LE, Mulhearn TO (1957) An experimental investigation of the deformed zone associated with indentation hardness impressions. J Mech Phys Solids 5(2):125–134. https://doi.org/10.1016/0022-5096(57)90056-X

Shukla P, Kumar V, Curtis M, Sondergeld CH, Rai CS (2013) Nanoindentation Studies on Shales. 47th US Rock Mechanics/Geomechanics Symposium 2:1194–1203

Tutuncu Azra N (1998) Nonlinear viscoelastic behavior of sedimentary rocks, part II: hysteresis effects and influence of type of fluid on elastic moduli. Geophysics 63(1):195–203

Tutuncu Azra N, Podiot Augusto L, Gregory Alvin R, Sharma Mukul M (1998) Nonlinear viscoelastic behavior of sedimentary rocks, part I: effect of frequency and strain amplitude. Geophysics 63(I):184–94

Vernik L, Liu XZ (1997) Velocity anisotropy in shales: a petrophysical study. Geophysics 62(2):521–532